Journal of Sound and Vibration (2002) **250**(2), 299–322
doi:10.1006/jsvi.2001.3867, available online at http://www.idealibrary.com on IDEAL®

EFFECTS OF END CAP AND ASPECT RATIO ON TRANSMISSION OF SOUND ACROSS A TRUSS-LIKE PERIODIC DOUBLE PANEL

M. EL-RAHEB

1000 *Oak Forest lane*, *Pasadena*, *CA* 91107, *U.S.A.*

AND

P. WAGNER

1020 *Crestview Drive*, *Pasadena*, *CA* 91107, *U.S.A.*

(*Received* 11 *September* 2000, *and in final form* 28 *June* 2001)

Transmission of sound across 2-D truss-like periodic double panels separated by an air gap and in contact with an acoustic fluid on the external faces is analyzed. Each panel is made of repeated cells. Combining the transfer matrices of the unit cell forms a set of equations for the overall elastic frequency response. The acoustic pressure in the fluids is expressed using a source boundary element method. Adding rigid reflecting end caps confines the air in the gap between panels which influences sound transmission. Measured values of transmission loss differ from the 2-D model by the wide low-frequency dip of the mass–spring–mass or "msm" resonance also termed the "air gap resonance". In this case, the panels act as rigid masses and the air gap acts as an adiabatic air spring. Results from the idealized 3-D and 2-D models, incorporating rigid cavities and elastic plates, reveal that the "msm" dip is absent in 2-D models radiating into a semi-infinite medium. The dip strengthens as aspect ratio approaches unity. Even when the dip disappears in 2-D, TL rises more steeply for frequencies above the "msm" frequency.

© 2002 Academic Press

1. INTRODUCTION

The sound isolation properties of a single truss-like periodic panel were studied in reference [1] by a 2-D model of a strip along its periodic axis (see Figure 1). Elastic frequency response of the strip made of repeated cells was expressed using transfer matrices of the unit cell developed in reference [2]. Acoustic pressure of the fluid was expressed using a source boundary element method developed in reference [3].

In a log–log plot, the envelope of transmission loss (TL) of the single panel excited by diffuse sound below coincidence varies linearly with frequency. Above the fundamental flexural resonance of the panel, TL is proportional to areal density of the panel, i.e., mass per unit length of the 2-D strip (see reference [3], equation (34)). As coincidence is approached from below, the envelope dips, reaching a minimum. When coincidence is crossed, the envelope rises again following a line with steeper slope than that below coincidence. To increase sound isolation further below coincidence, areal density must be increased. Alternatively, use of two lighter panels separated by an air gap may be adopted. The use of absorbing material in the air gap and boundary closures of the double panel is

0022-460X/02/070299 + 24 $35.00/0 © 2002 Academic Press

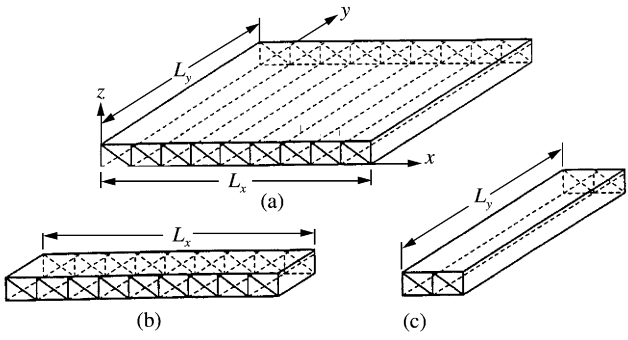

Figure 1. Panel with cell periodicity along one axis: (a) 3-D panel; (b) 2-D strip along x; (c) 3-D strip along y.

not desired in applications of sound isolation by polycarbonate panels where transparence or at least translucence is a requirement.

The transmission of sound across homogeneous double-leaf panels has been treated extensively in the literature. The most widely quoted is London [4], who employed the concepts of an infinite 2-D panel. Mulholland *et al.* [5] developed an analysis based on ray tracing of successive reflections in an infinite 2-D panel until intensity, reduced by transmission and damping, falls sufficiently. Although useful for preliminary screening of sound transmission, infinite panel theories are only approximate for finite panels. To address this deficiency, two other approaches were developed: multi-modal and statistical energy analysis. Sewell [6] applied multi-modal analysis to finite 2-D panels within rigid baffles. However, none of the 2-D methods of references [4–6] predict the dip in TL at the "msm" resonance. Price and Crocker [7] adopted statistical energy analysis to configurations including all constituents of a bounded environment. Statistical energy analysis succeeds only for configurations with high modal density and frequency. Guy [8] considered a square double plate backed by a rigid rectangular cavity adopting multi-modal analysis. Both elastic and acoustic fields were expanded in eigenfunctions satisfying certain constraints along the boundaries. The backing cavity reduces the geometry to a waveguide yielding to analysis. Radiation pressure on the excited plate was omitted, reducing its reactive loading. In turn, computed low-frequency resonances were slightly lower than those measured. Panneton and Noureddine [9] computed sound transmission across a finite double panel with poroelastic material filling the gap, adopting finite elements. They demonstrated that poroelastic material reduces the sharpness of the dip in TL at the "msm" frequency but does not eliminate it completely.

The sound isolation properties of the truss-like double panel are the subject of this study. A 2-D treatment is necessary in spite of the underlying approximations as a 3-D model of this complex geometry is intractable both analytically and numerically. Therefore, the objective of this work is the development of an analytical methodology, and the understanding of its limitations and drawbacks. Section 2 develops the hybrid model of elasto-acoustic frequency response of the two panels separated by an air gap. The model includes rigid reflecting caps confining the fluid in the cavity between panels. Section 3 derives 3-D and 2-D idealized models of double homogeneous plates with one of two possible end conditions: either backed by a rigid cavity or else radiating to a semi-infinite medium. The method uses modal expansions of the elastic plates and cavities, and a Green function boundary element method to model external radiation. The models in sections 2 and 3 are used on the same homogeneous double-leaf plate geometry for which experimental data were available. It was the discrepancy between the results of the model in

section 2 and the experimental data at the "msm" frequency that motivated the development of the models in section 3 to understand this phenomenon. Section 4 applies the model in section 2 to a baffled truss-like double panel in which fluids in the three regions do not mix. TL of the double panel is then compared with that of a single panel for different gap widths. Section 5 applies the model derived in section 2 to a homogeneous double panel made of glass and compares TL to experiment. A discrepancy in TL at the "msm" frequency emerges. Results from idealized 3-D and 2-D models derived in section 3, incorporating rigid cavities and flexible plates, reveal that the dip at the "msm" frequency disappears for a 2-D model radiating into a semi-infinite medium. Even for the 2-D model without a dip, TL rises more steeply above the "msm" frequency than in the single panel.

2. CONSTRUCTION OF THE HYBRID METHOD

The hybrid method is made of three steps. The first step uses transfer matrices of the repeated cell to form the global transfer matrix of a panel relating the ensemble of state vectors at all interfaces of cells to the external excitation, from known point forces and net acoustic pressure, applied at these interfaces. The second step uses influence coefficients to relate the source density applied over each segment to acoustic pressure and its normal gradient. The third step couples the elastic and acoustic fields by requiring continuity of acoustic and elastic velocities at the center of each segment.

2.1. ANALYSIS OF STRUCTURAL RESPONSE

The 2-D model of a panel strip along its periodic axis is shown in Figure 2. Each panel consists of N_c repeated rectangular cells. Cell n_c has four nodes connected by thin members and reinforced by a diagonal along side (1–4). The two faces of a panel are formed by connecting nodes (1–3) and (2–4) of all cells. Let $\mathbf{S}_{c12}(n_c)$ be the state vector of all forces and displacements along global coordinates at interfaces (1–2) of cell n_c,

$$S_{c12}(n_c) = \{\mathbf{f}_1, \mathbf{f}_2, \mathbf{g}_1, \mathbf{g}_2\}, \qquad \mathbf{f} = \{f_x, f_y, m_z\}^{\mathrm{T}}, \qquad \mathbf{g} = \{u_x, u_y, \theta_z\}^{\mathrm{T}}, \tag{1}$$

where forces, moments, displacements and rotations at corners 1 and 2 are shown in Figure 3. The cell transfer matrix $\mathbf{T}_c$ is defined as

$$\mathbf{S}_{c34}(n_c) = \mathbf{T}_{c12\text{-}34}(n_c) \cdot \mathbf{S}_{c12}(n_c). \tag{2}$$

Continuity of $\mathbf{S}_c$ at the interfaces of cells

$$\mathbf{S}_{c12}(n_c + 1) = \mathbf{S}_{c34}(n_c) \equiv \mathbf{T}_{c12\text{-}34}(n_c) \cdot \mathbf{S}_{c12}(n_c) \tag{3}$$

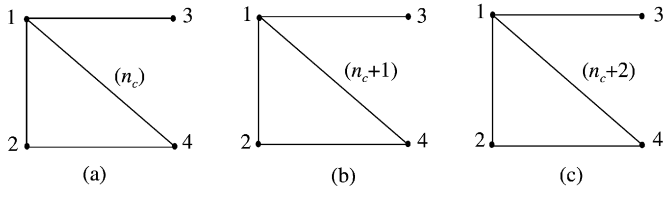

Figure 2. Corner convention of consecutive cells shown n_c, $(n_c + 1)$ and $(n_c + 2)$ disconnected: (a) cell (n_c); (b) cell $(n_c + 1)$; (c) cell $(n_c + 2)$.

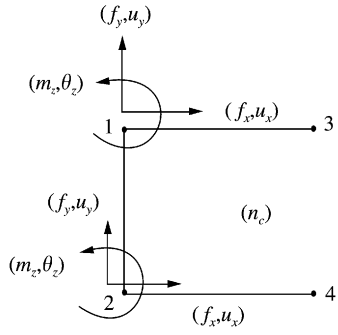

Figure 3. Cell state vector $S_{c12}(n_c)$ at interface n_c in global co-ordinates.

combined with constraints at the ends of the panel produces the global tri-diagonal transfer matrix $\mathbf{T}_G$ relating the global state vector $\mathbf{S}_G$ of the ensemble of state vectors at all interfaces of cells to the external excitation from known point forces and net acoustic pressure $\mathbf{F}_{G0}$:

$$\mathbf{T}_G\mathbf{S}_G = \mathbf{F}_{G0}, \quad \mathbf{S}_G = \{\mathbf{S}_{c1}, \mathbf{S}_{c2}, \ldots, \mathbf{S}_{cN_c+1}\}^{\mathrm{T}}, \quad \mathbf{F}_{G0} = \{\mathbf{F}_{10}, \mathbf{F}_{20}, \mathbf{0}, \mathbf{F}_{30}, \mathbf{0}, \ldots, \mathbf{0}, \mathbf{F}_{N_c+1,0}\}^{\mathrm{T}}, \tag{4a}$$

$$\mathbf{T}_G = \begin{bmatrix} -\mathbf{I} & \mathbf{Z}_1 & \mathbf{0} & \mathbf{0} & & & & & & \\ \mathbf{t}_{11}^1 & \mathbf{t}_{12}^1 & -\mathbf{I} & \mathbf{Z}_2 & & & & & & \\ \mathbf{t}_{21}^1 & \mathbf{t}_{22}^1 & \mathbf{0} & -\mathbf{I} & \mathbf{0} & \mathbf{0} & & & & \\ & & \mathbf{t}_{11}^2 & \mathbf{t}_{12}^2 & -\mathbf{I} & \mathbf{Z}_3 & & & & \\ & & \mathbf{t}_{21}^2 & \mathbf{t}_{22}^2 & \mathbf{0} & -\mathbf{I} & & & & \\ & & & & * & * & & & & \\ & & & & & & \mathbf{t}_{11}^N & \mathbf{t}_{12}^N & -\mathbf{I} & \mathbf{Z}_N \\ & & & & & & \mathbf{t}_{21}^N & \mathbf{t}_{22}^N & \mathbf{0} & \mathbf{I} \\ & & & & & & \mathbf{0} & \mathbf{0} & -\mathbf{I} & \mathbf{Z}_{N+1} \end{bmatrix}. \tag{4b}$$

In equation (4b),

$$\mathbf{T}_{cj} \equiv \begin{bmatrix} \mathbf{t}_{11}^j & \mathbf{t}_{12}^j \\ \mathbf{t}_{21}^j & \mathbf{t}_{22}^j \end{bmatrix}$$

are the four sub-matrices forming the transfer matrix of the jth cell $\mathbf{T}_{cj}$, $\mathbf{Z}_j$ is a (6×6) stiffness matrix connecting the jth interface to a fixed point in space, and $\mathbf{I}$ is the (6×6) unit matrix. Details of the derivation of $\mathbf{T}_c$ and $\mathbf{T}_G$ can be found in reference [2].

2.2. ANALYSIS OF ACOUSTIC PRESSURE

A source density of constant spatial intensity σ_j is distributed along the jth segment of each 2-D panel made of faces (1–3) or (2–4) of a cell as shown in Figure 4. Acoustic pressure and its normal gradient at the central point of the ith segment with unit normal n_i are

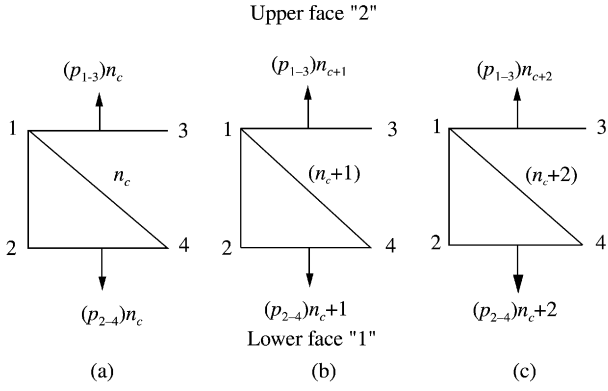

Figure 4. Acoustic pressure over segments on lower and upper faces of cells: (a) cell (n_c); (b) cell ($n_c + 1$); (c) cell ($n_c + 2$).

given by

$$p_i = \sum_{i=1}^{4N_c} A_{ij}\sigma_j, \quad \frac{\partial p_i}{\partial n_i} = \sum_{i=1}^{4N_c} B_{ij}\sigma_j, \tag{5a}$$

where the sum is over $4N_c$ segments formed by faces (1–3) and (2–4) of all cells in the double panel, and A_{ij}, B_{ij} are pressure and pressure gradient influence coefficients of the source density over the jth segment. In 2-D,

$$A_{ij} = -\frac{1}{2}\int_0^{s_j} [\mathrm{Y}_0(k_f r_{ij}) - \mathrm{i}\mathrm{J}_0(k_f r_{ij})]\,\mathrm{d}s, \quad i = \sqrt{-1}$$

$$B_{ij} = -\frac{k_f}{2}\int_0^{s_j} [\mathrm{Y}_1(k_f r_{ij}) - \mathrm{i}\mathrm{J}_1(k_f r_{ij})]\,\mathrm{d}s, \tag{5b}$$

$$r_{ij} = ((x_i - x_j)^2 + (y_i - y_j)^2)^{1/2}, \quad k_f = \omega/c_f,$$

where c_f is the speed of sound in the acoustic fluid, ω is the radian frequency, $s : (0 \leqslant s \leqslant s_j)$ is the intrinsic co-ordinate along the jth segment, and J_n, Y_n are the Bessel and Neuman functions. As $r \to 0$, $\mathrm{Y}_0(k_f r)$ has a $\ln(r)$ integrable singularity while $\mathrm{Y}_1(k_f r)$ has a $1/r$ singularity integrable in the form of a Cauchy principal value. Details of the derivation of A_{ij}, B_{ij} are included in reference [3].

2.3. ANALYSIS OF COUPLED RESPONSE

Consider the two baffled truss-like periodic 2-D panels in Figure 5. The two panels separate three distinct and unmixed volumes of fluid: fluid 1 fills the semi-infinite region below panel 1, fluid 2 fills the gap between panels 1 and 2, and fluid 3 fills the semi-infinite region above panel 2. Rigid reflecting end caps close the cavity containing fluid 2. Let faces "1" and "2" denote bottom and top faces of panel 1, and faces "3" and "4" the corresponding ones on panel 2 (see Figure 5).

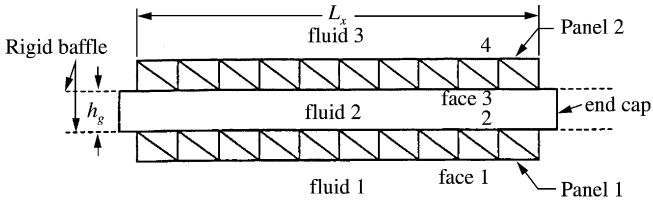

Figure 5. Double-leaf panel enclosing air gap.

Let $\bar{\mathbf{T}}_G$, $\bar{\mathbf{S}}_G$ denote the mechanically uncoupled global transfer matrix and state vector consolidating both panels 1 and 2,

$$\bar{\mathbf{T}}_G = \begin{bmatrix} \mathbf{T}_{G1} & \mathbf{0} \\ \mathbf{0} & \mathbf{T}_{G2} \end{bmatrix}, \quad \bar{\mathbf{S}}_G = \{\mathbf{S}_{G1}, \mathbf{S}_{G2}\}^{\mathrm{T}}, \tag{6a}$$

where $\mathbf{T}_{G1}$, $\mathbf{T}_{G2}$ have the form in equation (4b). Global dynamic equilibrium at all interfaces in the two panels is expressed by

$$\mathbf{T}_G \mathbf{S}_G = \mathbf{F}_{G0} = \bar{\mathbf{p}} + \bar{\mathbf{p}}_0 + \mathbf{F}_0, \tag{6b}$$

where $\bar{\mathbf{p}}$ are forces from acoustic pressure on all faces produced by motion of the panels and found in equation (5a), integrated over segments and acting at interfaces, $\bar{\mathbf{p}}_0$ are known forces from acoustic pressure generated by external acoustic sources, and $\mathbf{F}_0$ are external point forces. Expressing $\bar{\mathbf{p}}$ in terms of influence coefficients,

$$\bar{\mathbf{p}} = \bar{\mathbf{A}}_e \boldsymbol{\sigma}. \tag{7}$$

$\bar{\mathbf{A}}_e$ is the extended pressure influence coefficient matrix where in $\bar{\mathbf{A}}_e(i', j)$ all rows vanish except those corresponding to f_y in $\mathbf{S}_c$ (see equation (1)) in which case

$$\bar{\mathbf{A}}_e(i', j) = \mathbf{A}(i, j)\, \Delta l_i, \tag{7a}$$

where Δl_i is the length of the ith segment. The form (7a) assumes that acoustic elements are ordered as follows (see Figure 4):

$$\mathbf{p} = \{(p_{1-3})_1, (p_{1-3})_2, \ldots, (p_{1-3})_{N_c}, (p_{2-4})_{N_c}, (p_{2-4})_{N_c-1}, \ldots, (p_{2-4})_1\}^{\mathrm{T}}. \tag{7b}$$

The vector in equation (7b) applies to one panel. This means that the ordering of segments in each panel is such that pressures on top faces (1–3) of all cells are followed by pressures on bottom faces (2–4) of all cells along a panel strip in a clockwise sense. Since the three fluids are unmixed,

$$\bar{\mathbf{A}}_{e1,2} = \bar{\mathbf{A}}_{e1,3} = \bar{\mathbf{A}}_{e1,4} = \mathbf{0}, \quad \bar{\mathbf{A}}_{e2,1} = \bar{\mathbf{A}}_{e2,4} = \bar{\mathbf{A}}_{e3,1} = \bar{\mathbf{A}}_{e3,4} = 0, \quad \bar{\mathbf{A}}_{e4,1} = \bar{\mathbf{A}}_{e4,2} = \bar{\mathbf{A}}_{e4,3} = 0, \tag{7c}$$

where $\bar{\mathbf{A}}_{ep,q}$ denotes the influence of face p on face q. Substituting equations (7) into equations (6) determines $\bar{\mathbf{S}}_G$:

$$\bar{\mathbf{S}}_G = \bar{\mathbf{T}}_G^{-1} \bar{\mathbf{A}}_e \boldsymbol{\sigma} + \bar{\mathbf{S}}_0, \quad \bar{\mathbf{S}}_0 = \bar{\mathbf{T}}_G^{-1} \{\bar{\mathbf{p}}_0 + \mathbf{F}_0\}, \tag{8}$$

where $\bar{\mathbf{S}}_0$ is a state vector from external acoustic and mechanical excitation. Define $\mathbf{M}$ as

$$\mathbf{M} = \bar{\mathbf{T}}_G^{-1}\bar{\mathbf{A}}_e \tag{9}$$

and $\mathbf{W}$ as the reduced version of $\mathbf{M}$ including only rows which correspond to u_y in $\mathbf{S}_c$ (see equation (1)). The reduced equation (8) takes the form

$$\mathbf{w} = \mathbf{W}\boldsymbol{\sigma} + \mathbf{w}_0, \tag{10}$$

where $\mathbf{w}_0$ is the reduced vector of $\mathbf{S}_0$, including those rows in $\mathbf{W}$. Continuity of acoustic and elastic velocities normal to faces requires that

$$\rho_f \omega^2 \mathbf{w} = \frac{\partial \mathbf{p}}{\partial \mathbf{n}}, \tag{11}$$

where ρ_f is density of acoustic fluid. Invoking equation (5) in equation (11) yields

$$\rho_f \omega^2 \mathbf{w} = \mathbf{B}\boldsymbol{\sigma} + \mathbf{V}_0, \tag{12}$$

where $\mathbf{V}_0 = \partial \mathbf{p}_0/\partial \mathbf{n}$. Eliminating $\mathbf{w}$ from equations (10) and (12) yields

$$\left(\mathbf{W} - \frac{1}{\rho_f \omega^2}\mathbf{B}\right)\boldsymbol{\sigma} = \frac{1}{\rho_f \omega^2}\mathbf{V}_0 - \mathbf{w}_0, \tag{13}$$

which determines $\boldsymbol{\sigma}$; then $\mathbf{w}$ follows from equation (10).

3. 3-D MODEL OF DOUBLE PANEL BACKED BY A RIGID CAVITY, OR RADIATING INTO SEMI-INFINITE MEDIUM

Consider a square double panel made of two flexible homogeneous plates with side b, separated by an air gap of width h_g and backed by a rigid rectangular cavity. Using a co-ordinate system centered on the panel furthest from the cavity with sides b_c and depth h_c, as pictured in Figure 6, the gap volume is

$$\{x : 0 \leqslant x \leqslant h_g\} \otimes \{y : -b/2 \leqslant y \leqslant b/2\} \otimes \{z : -b/2 \leqslant z \leqslant b/2\} \tag{14a}$$

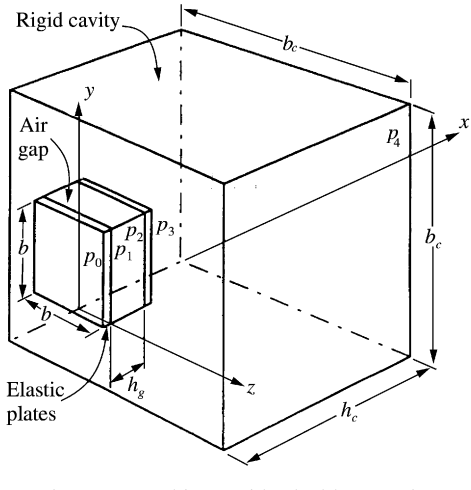

Figure 6. Double panel backed by a cavity.

while the backing cavity is

$$\{x : h_g \leqslant x \leqslant h_g + h_c\} \otimes \{y : -b_c/2 \leqslant y \leqslant b_c/2\} \otimes \{z : -b_c/2 \leqslant z \leqslant b_c/2\}. \quad (14b)$$

In both regions the acoustic pressure satisfies

$$\nabla^2 p + k_f^2 p = 0, \quad k_f = \omega/c_f. \quad (15)$$

In the gap volume, the pressure must obey boundary conditions on $|y| = b/2$ and $|z| = b/2$ so that

$$\left.\frac{\partial p}{\partial y}\right|_{|y|=b/2} = 0, \quad \left.\frac{\partial p}{\partial z}\right|_{|z|=b/2} = 0, \quad (16a)$$

while in the cavity the corresponding boundary conditions are

$$\left.\frac{\partial p}{\partial y}\right|_{|y|=b_c/2} = 0, \quad \left.\frac{\partial p}{\partial z}\right|_{|z|=b_c/2} = 0. \quad (16b)$$

On the first panel, compatibility of panel and acoustic velocities requires that

$$\left.\frac{\partial p}{\partial x}\right|_{x=0} = \rho_f \omega^2 w_1, \quad (17a)$$

while on the second panel it requires that

$$\left.\frac{\partial p}{\partial x}\right|_{x=h} = \rho_f \omega^2 w_2, \quad (17b)$$

where w_1, w_2 are panel displacements. Finally, the rigid back-wall of the cavity satisfies the condition

$$\left.\frac{\partial p}{\partial x}\right|_{x=h_g+h_c} = 0. \quad (17c)$$

For convenience, assume each panel "k" satisfies Euler's plate equation

$$(c_\varepsilon r_g)_k^2 \nabla^2 w_k - \omega^2 w_k = \Delta p_k(\rho_k h_k), \quad c_{\varepsilon k} = (E_k/\rho_k)^{1/2}, \quad r_{gk} = h_k/\sqrt{12}, \quad (18)$$

where Δp_k is the net acoustic pressure acting on the kth panel.

For pressures in the gap volume, define the normalized function

$$\varphi_m(y) = \bar{\bar{N}}_m^{-1/2} \cos\left[\frac{m\pi}{b}(y + b/2)\right]. \quad (19)$$

This satisfies the boundary condition at $|y| = b/2$. Also, $\varphi_m(z)$ happens to satisfy them at $|z| = b/2$. Then using these to expand the pressure,

$$p(x, y, z) = \sum_{m=0} \sum_{m'=0} (A_{mm'} \sin \alpha_{mm'} x + B_{mm'} \cos \alpha_{mm'} x)\, \varphi_m(y)\, \varphi_{m'}(z),$$
$$\alpha_{mm'} = \left(k_f^2 - \left(\frac{m\pi}{b}\right)^2 - \left(\frac{m'\pi}{b}\right)^2\right)^{1/2}. \quad (20)$$

For pressures within the cavity, the analogous function

$$\varphi_m^c(y) = \bar{\bar{N}}_m^{c\,-1/2} \cos\left[\frac{m\pi}{b_c}(y + b_c/2)\right] \tag{21}$$

satisfies the cavity boundary condition $|y| = b_c/2$. Thus the cavity pressure can be expanded as

$$\begin{gathered} p_c(x, y, z) = \sum_{m=0} \sum_{m'=0} (A_{mm'}^c \sin \alpha_{mm'}^c x + B_{mm'}^c \cos \alpha_{mm'}^c x)\, \varphi_m^c(y)\, \varphi_{m'}^c(z), \\ \alpha_{mm'}^c = \left(k_f^2 - \left(\frac{m\pi}{b_c}\right)^2 - \left(\frac{m'\pi}{b_c}\right)^2\right)^{1/2}. \end{gathered} \tag{22}$$

If each of the panels is simply supported, the deformations may also be expanded, this time in a series using

$$\psi_n(y) = \bar{\bar{N}}_n^{-1/2} \sin\left[\frac{n\pi}{b}(y + b/2)\right], \tag{23}$$

also normalized so that

$$w_k(y, z) = \sum_{n=1} \sum_{n'=1} w_{nn'}^k \psi_n(y) \psi_{n'}(z). \tag{24}$$

For each pair $\psi_n(y)\psi_{n'}(z)$ there is an eigenfrequency

$$\omega_{knn'} = (c_e r_g)_k \left[\left(\frac{n\pi}{b}\right)^2 + \left(\frac{n'\pi}{b}\right)^2\right]. \tag{25}$$

From the compatibility at the first panel,

$$\sum_{m=0} \sum_{m'=0} A_{mm'} \alpha_{nm'} \varphi_m(y) \varphi_{m'}(z) = \rho_f \omega^2 \sum_{n=1} \sum_{n'=1} w_{1nn'} \psi_n(y) \psi_{n'}(z), \tag{26a}$$

which leads to

$$A_{mm'} = \frac{\rho_f \omega^2}{\alpha_{mm'}} \sum_{n=1} \sum_{n'=1} N_{mn} N_{m'n'} w_{1nn'}, \quad m, m' \geqslant 0, \tag{26b}$$

using

$$\bar{N}_{mm'} = \int_{-b/2}^{b/2} \varphi_m^2(y)\, \mathrm{d}y \int_{-b/2}^{b/2} \varphi_{m'}^2(z)\, \mathrm{d}z = \bar{\bar{N}}_m \bar{\bar{N}}_{m'}, \quad \bar{\bar{N}}_m = \begin{cases} b & \text{if } m = 0, \\ b/2 & \text{if } m \neq 0, \end{cases} \tag{27}$$

$$N_{mn} = \int_{-b/2}^{b/2} \varphi_m(y)\, \psi_n(y)\, \mathrm{d}y = \begin{cases} 0, & \text{if } n = m + 2k,\ k = 0, 1, 2, \ldots, \\ \dfrac{2bn}{(n^2 - m^2)\pi}\, \bar{\bar{N}}_m^{-1/2} \bar{\bar{N}}_n^{-1/2}. \end{cases}$$

Form the compatibility at the second panel,

$$\sum_{m=0}\sum_{m'=0}\alpha_{mm'}(A_{mm'}\cos\alpha_{mm'}h_g - B_{mm'}\sin\alpha_{mm'}h_g)\varphi_m(y)\varphi_{m'}(z)$$

$$= \rho_f\omega^2\sum_{n=1}\sum_{n'=1} w_{2nn'}\psi_n(y)\psi_{n'}(z), \tag{28a}$$

which leads to

$$A_{mm'}\cos\alpha_{mm'}h_g - B_{mm'}\sin\alpha_{mm'}h_g$$

$$= \frac{\rho_f\omega^2}{\alpha_{mm'}}\sum_{n=1}\sum_{n'=1} N_{mn}N_{m'n'}w_{2nn'}, \qquad m, m' \geqslant 0. \tag{28b}$$

Substituting for $A_{mm'}$ from equation (27) yields

$$B_{mm'} = \frac{\rho_f\omega^2}{\alpha_{mm'}}\sum_{n=1}\sum_{n'=1} N_{mn}N_{m'n'}\left[\cot\alpha_{mm'}h_g\, w_{1nn'} - \cos\alpha_{mm'}h_g\, w_{2nn'}\right]. \tag{29}$$

Substituting equations (27) and (30) into equation (20) expresses p in terms of modal displacements alone in the gap volume,

$$p(x, y, z) = \sum_{m=0}\sum_{m'=0}\sum_{n=1}\sum_{n'=1}(w_{1nn'}\cos\alpha_{mm'}(h_g - x) - w_{2nn'}\cos\alpha_{mm'}x)$$

$$\times\frac{\rho_f\omega^2 N_{mn}N_{m'n'}}{\alpha_{mm'}\sin\alpha_{mm'}h_g}\varphi_m(y)\,\varphi_{m'}(z). \tag{30}$$

From the compatibility at the second panel,

$$\sum_{m=0}\sum_{m'=0}\alpha^c_{mm'}(A^c_{mm'}\cos\alpha^c_{mm'}h_g - B^c_{mm'}\sin\alpha^c_{mm'}h_g)\varphi^c_m(y)\varphi^c_{m'}(z)$$

$$= \rho_f\omega^2\sum_{n=1}\sum_{n'=1} w_{2nn'}\psi_n(y)\psi_{n'}(z), \tag{31}$$

which leads to

$$A^c_{mm'}\cos\alpha^c_{mm'}h_g - B^c_{mm'}\sin\alpha^c_{mm'}h_g$$

$$= \frac{\rho_f\omega^2}{\alpha^c_{mm'}}\sum_{n=1}\sum_{n'=1} N^c_{mn}N^c_{m'n'}w_{2nn'}, \qquad m, m' \geqslant 0;$$

$$N^c_{mn} = \int_{-b_c/2}^{b_c/2}\varphi^c_m(y)\,\psi^c_n(y)\,\mathrm{d}y = \begin{cases} 0, & \text{if } n = m + 2k,\ k = 0, 1, 2, \ldots, \\ \dfrac{2b_c n}{(n^2 - m^2)\pi}\,\bar{\bar{N}}^{c-(1/2)}_m\bar{\bar{N}}^{c-1/2}_n, \end{cases} \tag{32}$$

$$\bar{\bar{N}}^c_m = \begin{cases} b_c & \text{if } m = 0, \\ b_c/2 & \text{if } m \neq 0. \end{cases}$$

From the condition (17c) at the rigid wall of the cavity,

$$\sum_{m=0}\sum_{m'=0}\alpha^c_{mm'}(A^c_{mm'}\cos\alpha^c_{mm'}(h_g+h_c)-B^c_{mm'}\sin\alpha^c_{mm'}(h_g+h_c))\varphi^c_m(y)\varphi^c_{m'}(z)=0, \tag{33}$$

we find that

$$A^c_{mm'}=B^c_{mm'}\tan\alpha^c_{mm'}(h_g+h_c)$$

so that

$$\begin{Bmatrix}A^c_{mm'}\\B^c_{mm'}\end{Bmatrix}=\frac{\rho_f\omega^2}{\alpha^c_{mm'}\sin\alpha^c_{mm'}h_c}\sum_{n=1}\sum_{n'=1}N^c_{mn}N^c_{m'n'}w_{2nn'}\begin{cases}\sin\alpha^c_{mm'}(h_g+h_c),\\\cos\alpha^c_{mm'}(h_g+h_c).\end{cases} \tag{34}$$

Substituting equation (34) into equation (22) leads to

$$\begin{aligned}p_c(x,y,z)=&\sum_{m=0}\sum_{m'=0}\sum_{n=1}\sum_{n'=1}(w_{2nn'}\cos\alpha_{mm'}(h_g+h_c-x)\\&\times\frac{\rho_f\omega^2N^c_{mn}N^c_{m'n'}}{\alpha^c_{mm'}\sin\alpha^c_{mm'}h_c}\varphi^c_m(y)\,\varphi^c_{m'}(z).\end{aligned} \tag{35}$$

Substituting equation (24) into equation (18) yields

$$\sum_{n=1}\sum_{n'=1}w_{knn'}(\omega^2_{knn'}-\omega^2)\psi_n(y)\psi_{n'}(z)=\frac{\Delta p_k}{\rho_k h_k}. \tag{36}$$

Exploiting orthogonality of ψ_n produces

$$w_{knn'}(\omega^2_{knn'}-\omega^2)=\frac{1}{\rho_k h_k}\int_{-b/2}^{b/2}\int_{-b/2}^{b/2}\Delta p_k\psi_n(y)\psi_{n'}(z)\,\mathrm{d}y\,\mathrm{d}z. \tag{37}$$

For example, if on panel 1 pressure $p_0(y,\mathrm{z})$ acts on one side, while pressure $p(0,y,z)$ acts from the other side in the gap, then

$$\begin{aligned}\Delta p_1&=p_0(y,z)-p(0,y,z)\\&=p_0(y,z)-\sum_{m=0}\sum_{m'=0}\sum_{n=1}\sum_{n'=1}(w_{1nn'}\cos\alpha_{mm'}h_g-w_{2nn'})\\&\times\frac{\rho_f\omega^2N_{mn}N_{m'n'}}{\alpha_{mm'}\sin\alpha_{mm'}h_g}\varphi_m(y)\,\varphi_{m'}(z).\end{aligned} \tag{38}$$

Substituting equation (38) into equation (36) yields

$$\begin{aligned}w_{1nn'}(\omega^2_{1nn'}-\omega^2)=&\frac{1}{\rho_1h_1}\int_{-b/2}^{b/2}\int_{-b/2}^{b/2}p_0(y,z)\psi_n(y)\psi_{n'}(z)\,\mathrm{d}y\,\mathrm{d}z.\\&-\frac{1}{\rho_1h_1}\sum_{m=0}\sum_{m'=0}\sum_{p=1}\sum_{p'=1}(w_{1pp'}\cos\alpha_{mm'}h_g-w_{2pp'})\\&\times\frac{\rho_f\omega^2N_{mp}N_{m'p'}N_{mn}N_{m'n'}}{\alpha_{mm'}\sin\alpha_{mm'}h_g}.\end{aligned} \tag{39}$$

on the second panel,

$$\Delta p_2 = p(h_g, y, z) - p_c(h_g, y, z)$$

$$= \rho_f \omega^2 \sum_{m=0} \sum_{m'=0} \sum_{n=1} \sum_{n'=1} \left[(w_{1nn'} - w_{2nn'} \cos \alpha_{nm'} h_g) \times \frac{N_{mn} N_{m'n'}}{\alpha_{mm'} \sin \alpha_{mm'} h_g} \varphi_m(y) \varphi_{m'}(z) \right. \quad (40)$$

$$\left. - w_{2nn'} \cos \alpha^c_{mm'} h_c \times \frac{N^c_{mn} N^c_{m'n'}}{\alpha^c_{m'm'} \sin \alpha^c_{mm'} h_c} \varphi^c_m(y) \varphi^c_{m'}(z) \right].$$

Substituting equation (40) into equation (37) and enforcing orthogonality produces

$$w_{2nn'}(\omega^2_{2nn'} - \omega^2) = \frac{\rho_f \omega^2}{\rho_2 h_2} \sum_{m=0} \sum_{m'=0} \sum_{p=1} \sum_{p'=1}$$

$$\times \left[(w_{1pp'} - w_{2pp'} \cos \alpha_{mm'} h_g) \times \frac{N_{mp} N_{m'p'} N_{mn} N_{m'n'}}{\alpha_{mm'} \sin \alpha_{mm'} h_g} \right.$$

$$\left. - w_{2pp'} \cos \alpha^c_{mm'} h_c \times \frac{N^c_{mp} N^c_{m'p'} N^s_{mn} N^s_{m'n'}}{\alpha^c_{m'm'} \sin \alpha^c_{mm'} h_c} \right], \quad (41)$$

$$N^c_{mn} = \int_{-b_c/2}^{b_c/2} \varphi^c_m(y) \psi_n(y) \, dy, \quad N^s_{mn} = \int_{-b/2}^{b/2} \varphi^c_m(y) \psi_n(y) \, dy.$$

Since the integrals in equations (41) have the form given by equations (27) and since for the panel $\psi_n(y) = 0$ for $|y| > b/2$, then $N^c_{nm} = N^s_{mn}$. Define

$$u = \frac{m}{b_c} + \frac{n}{b}, \quad v = \frac{n}{b} - \frac{m}{b_c}, \quad u_0 = \frac{m}{2}\left(1 - \frac{b}{b_c}\right), \quad v_0 = \left(1 + \frac{b}{b_c}\right). \quad (42a)$$

Then

$$\bar{\bar{N}}^{c(1/2)}_m \bar{\bar{N}}^{1/2}_n = -\frac{1}{2\pi u}[\cos \pi(n + v_0) - \cos \pi u_0] - \frac{1}{2\pi v}[\cos \pi(n - v_0) - \cos \pi u_0]. \quad (42b)$$

For a finite set of functions in the expansions in equation (24), $n : \{1 \leqslant n \leqslant N_{mx}\}$, assign an index $i(n, n')$ to the pair (n, n') via

$$i(n, n') = n + (n' - 1) N_{mx}, \quad (43a)$$

which is invertible, i.e., for any "i", $(n_i, n_{i'})$ are also uniquely determined. Then we can assign to the vectors of unknowns $\{w_{1i}, w_{2i}, 1 \leqslant i \leqslant N_{mx}\}$ the values

$$w_{1i} = w_{1n_i n_i}, \quad w_{2i} = w_{2n_i n_i}. \quad (43b)$$

and similarly for the eigenfrequencies ω_{1i}, ω_{2i}. Based on this assignment, equations (39) and (41) can be cast in matrix form as follows:

$$[\mathbf{\Omega}^2_1 - \mathbf{I}\omega^2]\mathbf{w}_1 + \mathbf{M}_{11}\mathbf{w}_1 + \mathbf{M}_{12}\mathbf{w}_2 = \mathbf{F}, \quad [\mathbf{\Omega}^2_2 - \mathbf{I}\omega^2]\mathbf{w}_2 + \mathbf{M}_{21}\mathbf{w}_1 + \mathbf{M}_{22}\mathbf{w}_2 = \mathbf{0}, \quad (44a, b)$$

where

$$\mathbf{\Omega}^2_k = \text{diag}[\omega^2_{k1}, \omega^2_{k2}, \ldots, \omega^2_{kN_\omega}],$$

$$M_{11ij} = \frac{\rho_f \omega^2}{\rho_1 h_1} \sum_m \sum_{m'} \frac{N_{mn_j} N_{m'n'_j} N_{mn_i} N_{m'n'_i}}{\alpha_{mm'} \tan \alpha_{mm'} h_g} = \frac{\rho_2 h_2}{\rho_1 h_1} M_{22ij}, \tag{44c}$$

$$M_{12ij} = \frac{\rho_f \omega^2}{\rho_1 h_1} \sum_m \sum_{m'} \frac{N_{mn_j} N_{m'n'_j} N_{mn_i} N_{m'n'_i}}{\alpha_{mm'} \sin \alpha_{mm'} h_g} = \frac{\rho_2 h_2}{\rho_1 h_1} M_{21ij}.$$

Before solving equations (44) the forcing function **F** must be calculated. Assume that the first panel is excited by a plane wave at incidence with Euler angles (θ, θ') with pressure given by

$$p_0(y, z) = \bar{p}_0 \, \mathrm{e}^{\mathrm{i}\mathbf{k}\cdot\mathbf{r}} = \bar{p}_0 \mathrm{e}^{\mathrm{i}k_f (x \cos\theta \cos\theta' + y \sin\theta \cos\theta' + z \sin\theta')}, \tag{45}$$

which would be the case without radiation impedance on the side of the wave. Setting $x -> 0$ and substituting into equation (39) yields

$$F_i = \frac{1}{\rho_1 h_1 \bar{\bar{N}}_{n_i}^{1/2} \bar{\bar{N}}_{n_i}^{1/2}} f(n_i, k_f \cos\theta' \sin\theta) f(n'_i, k_f \sin\theta'),$$

$$f(n, \kappa) = \frac{(n\pi/b) \, \mathrm{e}^{-\mathrm{i}\kappa(b/2)}}{\kappa^2 - (n\pi/b)^2} [1 - (-1)^n \mathrm{e}^{\mathrm{i}\kappa b}]. \tag{46}$$

Substituting equations (46) into equations (44a, b) enables the solution for $w_1(y, z)$, $w_2(y, z)$, $p(x, y, z)$ and $p_c(x, y, z)$.

A particular measurement needed for comparison with experiment is transmission loss "TL",

$$\tau(\theta, \theta') = \frac{\iint p_g(h, y, z) \, v_g^*(h, y, z) \, \mathrm{d}y \, \mathrm{d}z}{\iint p_0(0, y, z) \, v_0^*(0, y, z) \, \mathrm{d}y \, \mathrm{d}z}, \tag{47}$$

where ()* stands for complex conjugate. For a plane wave described by equation (45), $v^* = (-(1/\mathrm{i}\omega\rho_f)(\partial p/\partial n))^*$. Therefore, the denominator in equation (47) becomes

$$\iint p_0(0, y, z) \, v_0^*(0, y, z) \, \mathrm{d}y \, \mathrm{d}y = \frac{b^2 \cos\theta \cos\theta'}{\rho_f c_f}. \tag{48}$$

The numerator in equation (47) requires calculating

$$-\mathrm{i}\omega \sum_{m,m'} \sum_{n,n'} w_{2nn'} \cos \alpha^c_{mm'} h_c \frac{N^c_{mn} N^c_{n'n'}}{\alpha^c_{mm'} \sin \alpha^c_{mm'} h_c}$$

$$\times \sum_{i,t'} \sum_{p,p'} w^*_{2pp'} \rho_f \omega^2 N^c_{tp} N^c_{t'p} \times \iint \varphi^c_m(y) \, \varphi^c_{m'}(z) \, \varphi^c_t(y) \, \varphi^c_{t'}(z) \, \mathrm{d}y \, \mathrm{d}z. \tag{49a}$$

Because these integrations are over $[-b/2, b/2] \times [-b/2, b/2]$, the orthogonality of the φ^c_m set is of no avail. Instead let

$$\int_{-b/2}^{b/2} \varphi^c_m(y) \, \varphi^c_n(y) \, \mathrm{d}y = D_{mn} \equiv [d(m+n) + d(m-n)] \, \bar{\bar{N}}_m^{c\,-(1/2)} \bar{\bar{N}}_n^{c\,-1/2},$$

$$d(m) = \begin{cases} b/2, & \text{if } m = 0, \\ \dfrac{b_c}{2m\pi}\left(\sin\dfrac{m\pi}{2b_c}(b_c + b) - \sin\dfrac{m\pi}{2b_c}(b_c - b)\right). \end{cases} \tag{49b}$$

Using equation (49b) in equation (49a), the numerator of equation (47) becomes

$$\frac{1}{\mathrm{i}} \sum_{m,m'} \sum_{t,t'} \frac{\rho_f \omega^3 D_{mt} D_{m't'}}{\alpha^c_{mm'} \tan \alpha^c_{mm'} h_c} \left\{ \sum_{n,n'} w_{2nn'} N^c_{mn} N^c_{m'n'} \right\} \left\{ \sum_{p,p'} w^*_{2pp'} N^c_{tp} N^c_{t'p'} \right\}. \tag{50}$$

For a diffuse field, transmission loss is defined as

$$\tau_D = \iint \tau(\theta, \theta') \cos\theta \, \mathrm{d}\theta \, \mathrm{d}\theta'. \tag{51}$$

When dimensions of the cavity approach infinity, a radiation condition replaces the eigenmode expansion in equation (30) to describe acoustic pressure:

$$p_c(x, y, z) = \iint G(x - h_g, y - \eta, z - \zeta) \frac{\partial p_c(h_g, \eta, \zeta)}{\partial n} \, \mathrm{d}\eta \, \mathrm{d}\zeta, \tag{52}$$

where $G = \mathrm{e}^{\mathrm{i}k_f r}/r$ and $r^2 = (x - h_g)^2 + (y - \eta)^2 + (z - \zeta)^2$, where the integrations are over the panel dimensions $-b/2 \leqslant \eta, \varsigma \leqslant b/2$. The boundary condition at the panel surface yields

$$\frac{\partial p_c(h_g, \eta, \varsigma)}{\partial n} = \rho_f \omega^2 w_2 \equiv \rho_f \omega^2 \sum_n \sum_{n'} w_{2nn'} \psi_n(y) \psi_{n'}(z), \tag{53a}$$

$$p_c(x, y, z) = \rho_f \omega^2 \sum_n \sum_{n'} w_{2nn'} \iint G(x - h, y - \eta, z - \zeta) \, \psi_n(\eta) \psi_{n'}(\varsigma) \, \mathrm{d}\eta \, \mathrm{d}\zeta. \tag{53b}$$

Equation (53a) modifies matrices $\mathbf{M}_{11}$ and $\mathbf{M}_{22}$ in equations (44) to include radiation:

$$\begin{aligned} M_{22ij} &= \frac{\rho_f \omega^2}{\rho_2 h_2} \iiiint G(0, \eta - \eta', \zeta - \zeta') \, \psi_{nj}(\eta) \, \psi_{n'j}(\zeta) \\ &\quad \times \psi_{ni}(\eta') \, \psi_{n'i}(\zeta') \, \mathrm{d}\eta \, \mathrm{d}\zeta \, \mathrm{d}\eta' \, \mathrm{d}\zeta' \\ &= \frac{\rho_1 h_1}{\rho_2 h_2} M_{11ij}. \end{aligned} \tag{54}$$

The quadruple integral in equation (54) can be converted to a double integral by an appropriate transformation derived in Appendix A.

In the 2-D treatment, the co-ordinate system is similar to that used in 3-D, except that the z-axis is lost. Therefore, all expressions for displacement and pressure include one sum and no z dependence. The derivations are omitted for brevity.

4. RESULTS OF TRUSS-LIKE 2-D DOUBLE PANEL

The hybrid method developed in section 2 is applied to both single and double 2-D panels with cell geometry listed in Table 1 where (l, h) are length and thickness of each

TABLE 1

Panel geometry

Member	l(cm)	h(cm)
(1–3)	1·50	0·10
(1–2)	1·62	0·06
(2–4)	1·50	0·10
(1–4)	2·21	0·03

member (see Figure 2). All panels are made of polycarbonate with material properties $E = 2{\cdot}3 \times 10^9$ Pa, $\rho = 1{\cdot}2$ g/cm^3, where E, ρ are Young's modulus and mass density. Each panel has areal density 3·7 kg/m^2 and is 1·2 m long with 80 cells. The two panels are simply supported at the ends and include viscoelastic damping in the form of a complex modulus $E_c = E(1 + 0{\cdot}02\mathrm{i})$. The acoustic fluid is air with $\rho_f = 1{\cdot}225 \times 10^{-3}$ g/cm^3 and $c_f = 340$ m/s.

Define

$$TL^D = 10 \log_{10} \left| \int_0^{\pi/2} TL^\theta \cos\theta \, \mathrm{d}\theta \right|, \quad TL^\theta = \frac{L_x \cos\theta}{\rho_f c_f} R_e \int_0^{L_x} pv^* \, \mathrm{d}s. \tag{55}$$

Here TL^D is the transmission loss from diffuse sound in dB, TL^θ is the ratio of transmitted to incident acoustic energy, (p, v^*) are the acoustic pressure and complex conjugate of acoustic velocity, and L_x is the length of panel. For the double panel, (p, v^*) is evaluated on face 4, while for the single panel it is evaluated on face 2.

Figures 7(a–c) plot TL^D against Ω for the double panel and for three gap widths $h_g = 3$, 6 and 10 cm, in the frequency range $100 \leqslant \Omega \leqslant 6000$ Hz. For each h_g, TL^D of the single panel is also plotted. Also indicated are resonances Ω_{T1}, Ω_{T2}, etc., which are acoustic resonances across the air gap between panels. At low frequencies, the envelope of TL^D for the double panel rises in parallel with that of the single panel and exceeds it by approximately 6 dB per octave as expected from known results of the homogeneous double leaf. As long as both panels move in phase, the areal density of the double panel is twice that of the single panel explaining the 6 dB shift. When the "msm" frequency is crossed, the two panels move out of phase allowing the TL^D of the double panel to rise more steeply than the single panel for frequencies below coincidence near 4000 Hz (see Figure 3 of reference [1]). In fact, for the single panel, TL^D rises approximately by 6 dB per octave, while TL^D for the double panel rises by 12 dB per octave, consistent with results in reference [10]. In all TL^Ds of Figure 7, there is no evidence of the dip at the "msm" frequency. The circumstances under which the "msm" dip is absent or greatly attenuated will be investigated in section 5. Increasing h_g raises TL^D but not proportionately.

The presence of rigid end caps enables standing waves to be created within the air gap at frequencies $\Omega_{Ln} = nc_f/(2L_x)$ appearing as dips in TL^D where L_x is panel length. Larger gaps strengthen the dips because of larger reflective surface. Smaller gaps weaken the dips to the point of vanishing. Remote from the dips, TL^D is unaffected by end caps. To demonstrate this, TL^D is computed for a double plate each with the same areal density as the truss-like panel in Table 1 in the frequency range $50 \leqslant \Omega \leqslant 500$ Hz and for $h_g = 3$, 6 and 10 cm. Figure 8(a) plots TL^D for $h_g = 3$ cm. In this case Ω_{L2} appears at 200 Hz while Ω_{L3} appears at 400 Hz as a wide dip. For $h_g = 6$ cm (see Figure 8(b)), both Ω_{L2} and Ω_{L3} appear at 250 and 410 Hz, respectively, as sharp dips indicating stronger resonances. For $h_g = 10$ cm (see

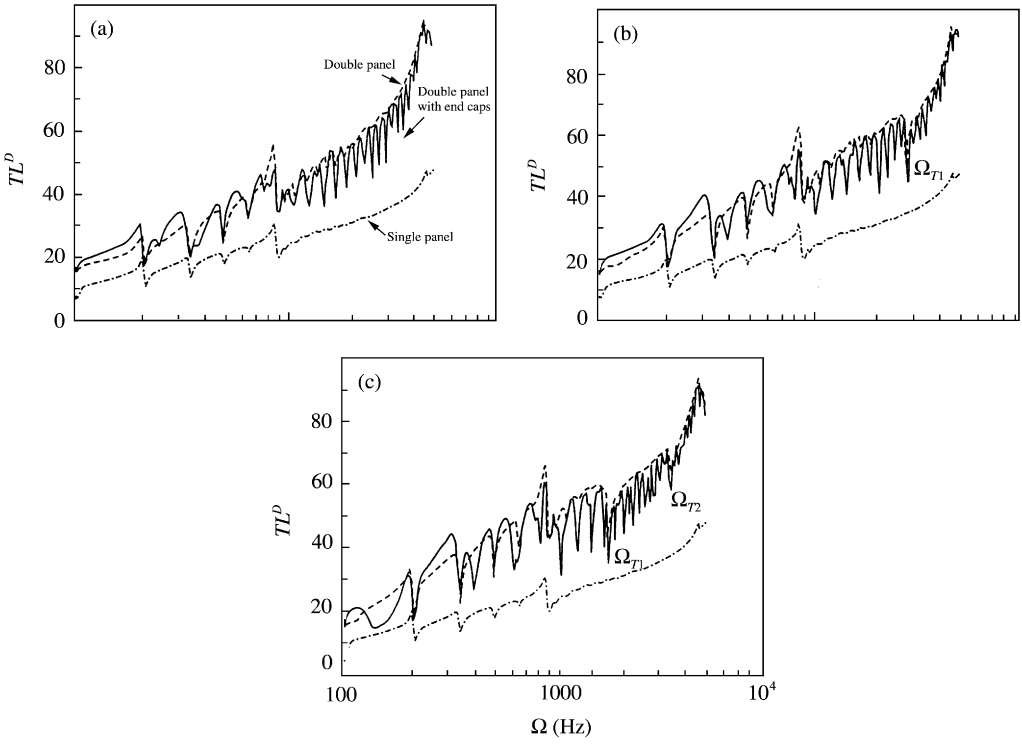

Figure 7. TL^D across truss-like periodic panel (3·5 kg/m^2, $L_x = 0{\cdot}75$ m): – – – –, double panel separated by air gap h_g; ——, double panel with end caps; –·–·–·–·–, single panel: (a) $h_g = 3$ cm; (b) 6 cm; (c) 10 cm.

Figure 8(c), $\Omega_{L2} = 280$ Hz and $\Omega_{L3} = 420$ Hz and the dips are sharper still. Sharp resonances in Figure 8(c) shift to lower frequencies and become less pronounced as the air gap is reduced. This is indicative of acoustic damping due to the compliance of the panels. The higher the aspect ratio L_x/h_g the more effective wall compliance becomes and the weaker the standing wave.

5. RESULTS OF HOMOGENEOUS DOUBLE PLATE

In contrast to measured results which will be presented later, the 2-D model did not exhibit the strong dip at the "msm" frequency, although a simple 1-D model of two masses separately by an adiabatic fluid spring predicts the "msm" (see reference [10]). Since the only available experimental results were for the homogeneous double plate, an equivalence was constructed to allow modelling it. The 2-D model of section 2 was used to compute results for the homogeneous double plate by appropriate choice of cell dimensions in the truss-like panel. Let (w_c, h_c) be the width and height of a cell and h_i, $i = 1, 4$, the thickness of each member in a cell (see Figure 3). To construct an equivalent truss-like panel with the same mass and stiffness as the homogeneous plate of thickness h_p, assume the same modulus E and density ρ. Equating areal density and radius of gyration yields

$$h_p = \frac{(2h_1 w_c + h_3 h_c)}{w_c}, \quad \frac{h_p^3}{12} = \frac{h_1^3}{6} + \frac{h_1 h_c^2}{2}. \tag{56}$$

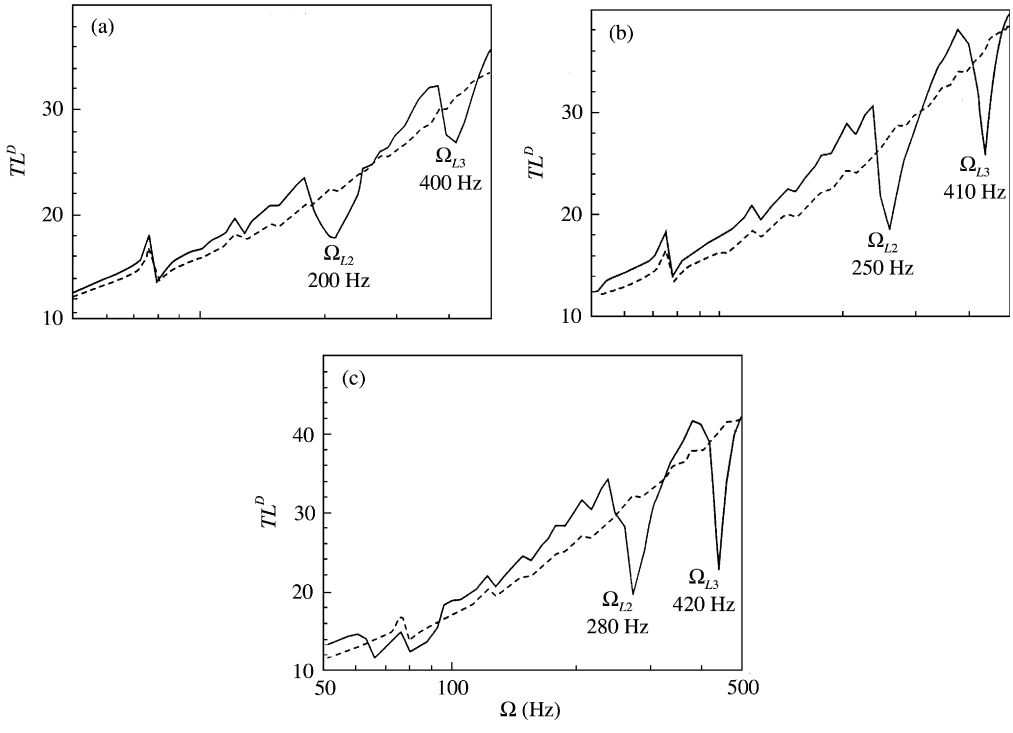

Figure 8. Effect of end caps and gap width on TL^D for a homogeneous double panel (3·5 kg/m^2, $L_x = 1$ m): ------, no end caps; ——, with end caps; (a) $h_g = 3$ cm; (b) 6 cm; (c) 10 cm.

Given (w_c, h_c, h_p), equation (56) is solved for h_1 and h_3. Preferably, h_c should be much smaller than w_c provided $h_3 > 0$. To strengthen shear stiffness of the cell, a diagonal element is added with reduced density to keep equation (56) valid and with increased modulus to reduce shear deformation and raise the diagonal's resonances over those of the other members.

TL^D was measured for the square double panel made of glass with dimensions 1·4 m × 1·4 m and thickness 5 mm separated by a 1·2 cm air gap. These measurements were performed by Peutz and Associates in the Netherlands (see reference [11]). TL^D was calculated by the 2-D model in section 2 assuming an equivalent truss-like panel according to equation (56). Figure 9 compares experimental and analytical TL^D, the latter with and without end caps. In this figure, the number of computed points is only three times the number of experimental points for consistent comparison. The average lines of experiment and theory are in overall agreement. The fundamental structural resonance of the panels occurs below 100 Hz outside the range in Figure 9. The strong and wide dip near 3000 Hz is at coincidence. The discrepancy is greatest around the experimentally observed dip centered at 230 Hz. To identify the nature of this dip, consider the two possible explanations:

(1) symmetric acoustic standing wave Ω_{L2} along the panel in the air gap,

$$\Omega_{L2} = c_f/L_x \simeq 243 \text{ Hz}; \tag{57a}$$

(2) "msm" resonance $\Omega_{msm} \simeq \dfrac{c_f}{2\pi}\left(\dfrac{\rho_f}{\rho h_g}\left(\dfrac{1}{h_1}+\dfrac{1}{h_2}\right)\right)^{1/2} \simeq 223 \text{ Hz}.$ (57b)

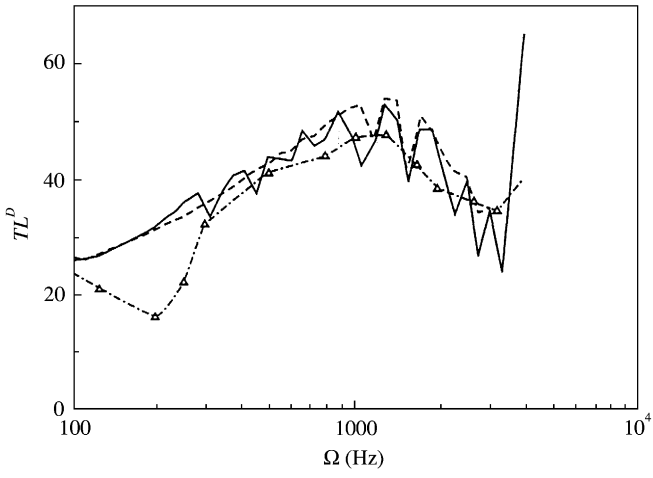

Figure 9. TL^D across homogeneous double-leaf glass plates (25 kg/m^2, $L_x = 1{\cdot}4$ m, $h_1 = h_2 = 5$ mm, $h_g = 1{\cdot}2$ cm): ——, 2-D theory with end caps; – – –, 2-D theory, no end caps; –·–△–·–, experiment.

To rule out the first possibility, TL^D was computed for panel lengths: $L_x = 50$, 75 and 100 cm. Ω_{L2} is identified by the missing dip in the uncapped configuration. The nominal Ω_{L2} is that computed by the 1-D expression in equation (57b). For 50 cm, the nominal Ω_{L2} at 694 Hz corresponds to a wide and strong dip as shown in Figure 10(a). For 75 cm, Ω_{L2} shifts to 430 Hz and the dip is weak and narrow (see Figure 10(b)). For 100 cm, the Ω_{L2} dip is absent. This demonstrates that the Ω_{L2} dip weakens with L_x/h_g, vanishing completely at $L_x = 1$ m, as shown in Figure 10(c). This eliminates Ω_{L2} as the cause of the experimental dip at 230 Hz.

To investigate the circumstance under which the dip at the "msm" frequency disappears, the idealized 3-D and 2-D models derived in section 3 were used. Results in Figure 11 were computed at smaller frequency intervals than those in Figure 9 for a closer comparison between the two models. For this reason, the TL^D lines for the same geometry may seem different in these two figures. Figure 11(a) plots TL^D from the 2-D and 3-D models for the double plate backed by a rigid cavity with 150 cm side length and 150 cm depth. Both 2-D and 3-D models predict a weak dip in TL^D at Ω_{msm}. Figure 11(b) plots TL^D from the 2-D and 3-D models for the double plate radiating into a semi-infinite medium. While the 3-D model predicts a strong dip at Ω_{msm}, the 2-D model shows only a weak dip at that frequency, comparable to that when the double plate is backed by a rigid cavity. It follows that the dip at Ω_{msm} is strong only in 3-D when the double panel radiates into a semi-infinite medium. Since the 2-D model is the limit of the 3-D model when aspect ratio of the panel L_y/L_x (Figure 1) becomes infinite, it is expected that the dip will weaken as this aspect ratio departs from unity. Also, the Ω_{L2} dip becomes weaker as the aspect ratio L_x/h_g (Figure 5) increases. Even when the dip is weak, crossing the Ω_{msm} causes a phase change in the pressure across the gap exhibited by the steeper TL^D. Each coupled elasto-acoustic structural resonance is followed by a Ω_{msm} frequency. The frequency interval separating them is widest at the fundamental Ω_{msm} given by relation (57b), then diminishes for all following pairs of Ω_L and Ω_{msm}.

Models in section 3 based on an entirely different approach point to the same underlying cause: *aspect ratio*. The reasonable agreement between the different models, with the exception of Ω_{msm}, suggests the limit of applicability of the 2-D model. Figure 12 compares TL^D of the glass double glaze from the 2-D models in section 2 with and without end caps,

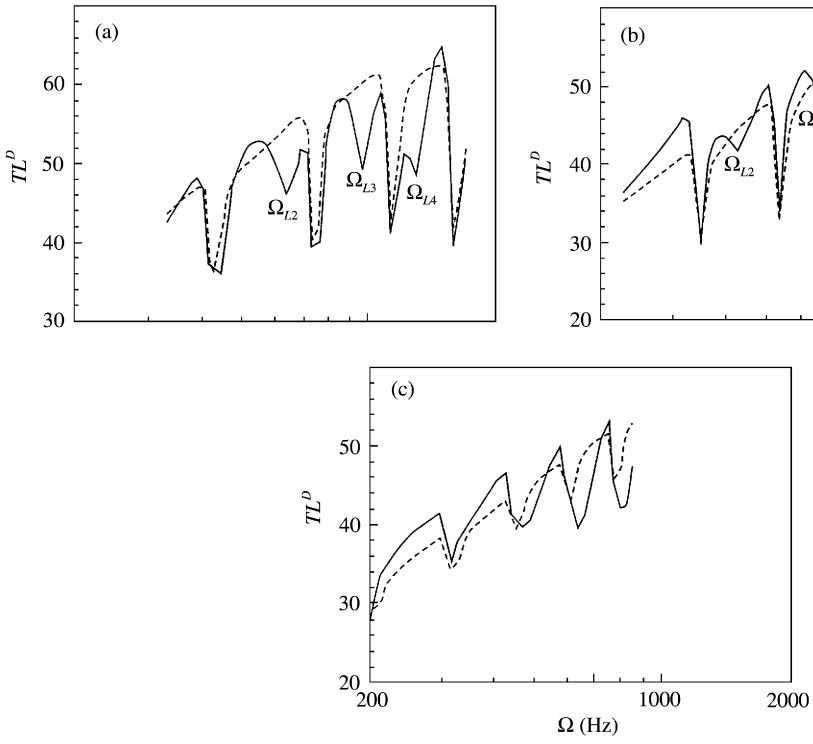

Figure 10. Effect of panel length on TL^D across homogeneous double-leaf glass plates with end caps (25 kg/m^2, $h_g = 1{\cdot}2$ cm): ——, capped; – – – –, uncapped: (a) $L_\kappa = 49$ cm; (b) 74·2 cm; (c) 99·4 cm.

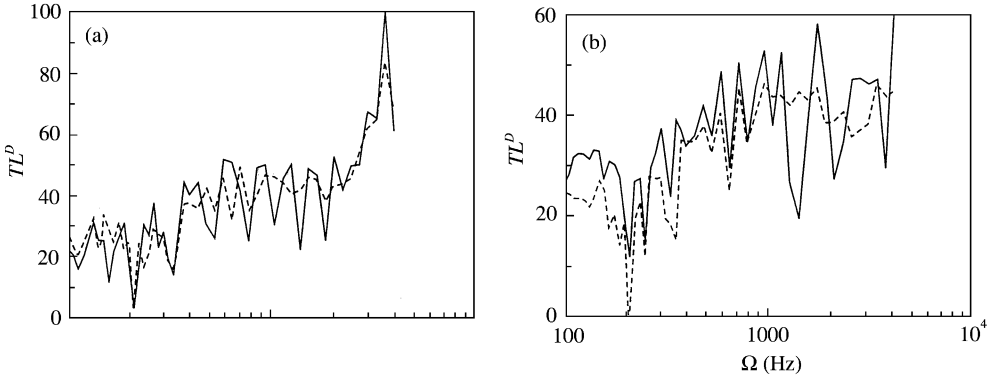

Figure 11. TL^D across homogeneous double-leaf glass plates (25 kg/m^2, $L_x = L_y = 1{\cdot}4$ m, $h_1 = h_2 = 5$ mm, $h_g = 1{\cdot}2$ cm): (a) backed by rigid $1{\cdot}5 \times 1{\cdot}5 \times 1{\cdot}5$ m^3 cavity; (b) radiating into a semi-infinite medium.

TL^D from the 3-D model radiating into a semi-infinite medium in section 3, and once more the experiment averaged over a 1/3-octave band. As with Figure 9, the resolution in Figure 12 is coarser than that in Figure 11 to be consistent with the experimental data. The average TL of the 2-D models are higher than those of the 3-D model because in 2-D radiation damping is increased due to the lack of variation of pressure along the infinite direction. In other words, acoustic impedance, defined as pressure induced by a unit velocity, of a 2-D strip is smaller than that of a 3-D square panel with side equal to strip

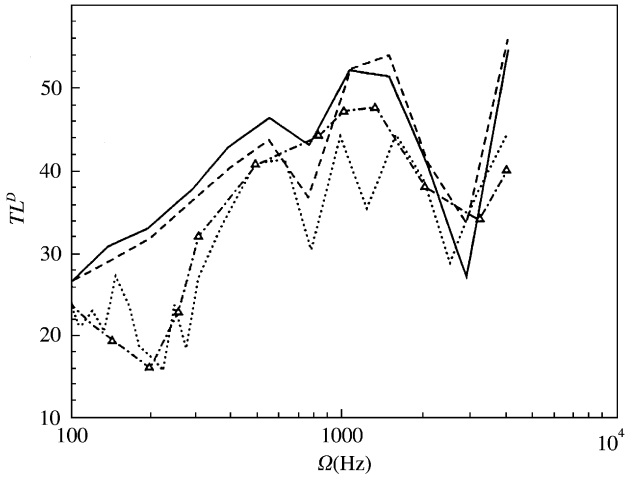

Figure 12. TL^D across homogeneous double-leaf glass plates (25 kg/m^3, $L_x = L_y = 1{\cdot}4$ m, $h_1 = h_2 = 5$ mm, $h_g = 1{\cdot}2$ cm): ——, 2-D analysis (with end caps); – – –, 2-D analysis (no end caps); · · · ·, 3-D analysis (with end caps); –·–△–·–, experiment.

length (see Figures 5 and 6 of reference [12]). The quantitative agreement between 3-D model and experiment near Ω_{msm} is satisfactory, and the average lines with filtered resonances for all models differ by approximately 3 dB elsewhere. This comparison confirms that a 3-D treatment is needed to predict the wide Ω_{msm} dip when L_y/L_x is near unity. In spite of its limitations, the 2-D model is the only model practical for the truss-like double panel since the 3-D model is intractable both analytically and numerically due to the cellular construction.

6. CONCLUSION

A hybrid model is developed to analyze transmission of sound across a 2-D truss-like periodic panel. Analysis proceeds through elastic response using transfer matrices of the unit cell and through acoustic response using 2-D boundary elements. Also developed are idealized 3-D and 2-D models incorporating rigid walls and flexible plates, backed by a rigid cavity or radiating into a semi-infinite medium, adopting a modal solution. Noteworthy results from the double panels are the following.

(1) Below coincidence and above the "msm" frequency Ω_{msm}, the 2-D model shows that TL^D of the double panel has a steeper slope than that of the single panel consistent with measurement, but excludes the wide dip in TL^D at Ω_{msm} observed in 3-D.
(2) The dip in TL^D at Ω_{msm} disappears in all models other than the 3-D geometry radiating into a semi-infinite medium. Based on the comparison between 2-D and 3-D models, it is expected that the dip at Ω_{msm} would weaken when aspect ratio L_y/L_x departs from unity.
(3) Rigid reflecting end caps induce standing waves along the panel, which appear as dips in TL^D. These dips weaken with aspect ratio L_x/h_g, and ultimately vanish when that ratio is over 100.

(4) Taking aspect ratio into account resolves the discrepancy between results of the 2-D and 3-D models radiating into semi-infinite medium.
(5) Comparison of the different models identifies the limitations of the 2-D model, an unavoidable trade-off for the truss-like panel, as a 3-D treatment is intractable.

REFERENCES

1. M. EL-RAHEB and P. WAGNER 1997 *Journal of the Acoustical Society of America* **102**, 2176–2183. Transmission of sound across a truss–like periodic panel; 2-D analysis.
2. M. EL-RAHEB 1997 *Journal of the Acoustical Society of America* **101**, 3457–3465. Frequency response of a truss–like periodic panel; 2-D analysis.
3. M. EL-RAHEB 1997 *Journal of the Acoustical Society of America* **102**, 955–967. Elasto-acoustics of a two-dimensional thin strip by a hybrid method.
4. A. LONDON 1950 *Journal of the Acoustical Society of America* **22**, 270–276. Transmission of reverberant sound through double walls.
5. K. MULHOLLAND, H. PARBROOK and A. CUMMINGS 1967 *Journal of Sound and Vibration* **6**, 324–329. Transmission loss of double panels.
6. E. SEWELL 1970 *Journal of Sound and Vibration* **12**, 33–39. Two-dimensional solution for transmission of reverberant sound through a double partition.
7. J. PRICE and M. CROCKER 1970 *Journal of the Acoustical Society of America* **47**, 683–691. Sound transmission through double panels using statistical energy analysis.
8. R. GUY 1981 *Acustica* **49**, 323–333. The transmission of airborn sound through a finite panel, air gap, panel and cavity configuration—a steady state analysis.
9. R. PANNETON and N. ATALLA 1996 *Journal of the Acoustical Society of America* **100**, 346–354. Numerical prediction of transmission through finite multiplayer systems with poroelastic materials.
10. F. FAHY 1974 *Sound and Structural Vibration, Radiation Transmission and Response*. New York: Academic Press, Harcourt Brace Jovanovich Publishers: first edition, 167–172.
11. M. VERKAMEN 1995 *Laboratory Measurements of Airborn Sound Insulation According to ISO* 140–3: 1995 *of Double Panel Glass Sheet*. The Netherlands: Peutz and Associates consulting firm B. V.
12. M. EL-RAHEB 1997 *Journal of the Acoustical Society of America* **102**, 955–967. Elasto-acoustics of a two-dimensional thin strip by a hybrid method.

APPENDIX A: TRANSFORMATION OF 3-D MODAL PRESSURE COEFFICIENTS

Numerical evaluation of the quadruple integrals of the 3-D modal pressure coefficients in equation (54) is computationally prohibitive. An alternative relies on a transformation of co-ordinates enabling the evaluation of two integrals analytically. Start with the integral in equation (54):

$$\Im = \iiiint G(\eta - \eta', \zeta - \zeta') f(n_1, \eta) f(n_2, \eta') f(n_3, \zeta) f(n_4, \zeta') \, \mathrm{d}\eta \, \mathrm{d}\eta' \, \mathrm{d}\zeta \, \mathrm{d}\zeta', \tag{A1}$$

where $f(n_i, x)$ can be integrated analytically. Change to the new set of co-ordinates

$$\alpha = \eta - \eta', \quad \alpha' = \eta - \eta', \quad \beta = \zeta - \zeta', \quad \beta' = \zeta - \zeta', \tag{A2}$$

in which $G(\alpha, \beta)$ is independent of α' and β' so those integrations may be performed analytically, reducing equations (A2) to a double integral evaluated numerically.

In $(\alpha, \beta, \alpha', \beta')$ co-ordinates,

$$\mathrm{d}\eta \, \mathrm{d}\eta' \, \mathrm{d}\zeta \, \mathrm{d}\zeta' = \left| \frac{\partial(\eta, \eta')}{\partial(\alpha, \alpha')} \right\| \frac{\partial(\zeta, \zeta')}{\partial(\beta, \beta')} \left| \mathrm{d}\alpha \, \mathrm{d}\alpha' \, \mathrm{d}\beta \, \mathrm{d}\beta' = \frac{1}{4} \mathrm{d}\alpha \, \mathrm{d}\alpha' \, \mathrm{d}\beta \, \mathrm{d}\beta'. \right. \tag{A3}$$

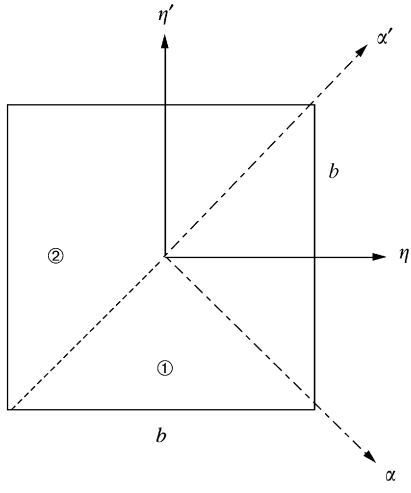

Figure A1. Rotated co-ordinate system and regions of integration.

To describe the region of integration in the new co-ordinate system, consider the $(\eta, \eta'; \alpha, \alpha')$ at first and then recognize that $(\zeta, \zeta'; \beta, \beta')$ is identical in form. Figure A1 shows a square with side length b, divided into two regions (1) and (2). The integral will be performed separately in each region.

Boundary region (1)

$$\text{Lower bound, innermost } (\alpha'): \eta = -\frac{b}{2} \Rightarrow \alpha' = -b - \alpha.$$

$$\text{Upper bound, innermost } (\alpha'): \eta' = \frac{b}{2} \Rightarrow \alpha' = b + \alpha.$$

$$\text{Outermost } (\alpha): \left[\left\{\eta = -\frac{b}{2}, \eta' = \frac{b}{2}\right\}, \left\{\eta = -\frac{b}{2} = \eta'\right\}\right] \quad \text{or } [-b, 0].$$

Boundary of region (2)

$$\text{Lower bound, innermost } (\alpha'): \eta = -\frac{b}{2} \Rightarrow \alpha' = -b + \alpha.$$

$$\text{Upper bound, innermost } (\alpha'): \eta' = \frac{b}{2} \Rightarrow \alpha' = b - \alpha.$$

$$\text{Outermost } (\alpha): \left[0, \left\{\eta = \frac{b}{2}, \eta' = -\frac{b}{2}\right\}\right] \quad \text{or } [-b, 0].$$

The quadruple integral $\mathfrak{I}$ is split into four parts:

$$\mathfrak{I} = \frac{1}{4}\int_{-b}^{0}\int_{-b-\beta}^{b+\beta}\int_{-b}^{0}\int_{-b-\alpha}^{b+\alpha} \Phi \, d\alpha' \, d\alpha \, d\beta' \, d\beta + \frac{1}{4}\int_{-b}^{0}\int_{-b-\beta}^{b+\beta}\int_{0}^{b}\int_{-b+\alpha}^{b-\alpha} \Phi \, d\alpha' \, d\alpha \, d\beta' \, d\beta$$

$$+\frac{1}{4}\int_0^b\int_{-b+\beta}^{b-\beta}\int_{-b}^{0}\int_{-b-\alpha}^{b+\alpha}\Phi\,\mathrm{d}\alpha'\,\mathrm{d}\alpha\,\mathrm{d}\beta'\,\mathrm{d}\beta+\frac{1}{4}\int_0^b\int_{-b+\beta}^{b-\beta}\int_0^b\int_{-b+\alpha}^{b-\alpha}\Phi\,\mathrm{d}\alpha'\,\mathrm{d}\alpha\,\mathrm{d}\beta'\,\mathrm{d}\beta$$

$$=Q_1+Q_2+Q_3+Q_4. \tag{A4}$$

The innermost integrals, formerly $\iint \mathrm{d}\eta'\,\mathrm{d}\eta$, reduce to $\int f(n_1,\eta)\,f(n_2,\eta')\,\mathrm{d}\alpha'$, but $\eta=(1/2)(\alpha+\alpha')$, $\eta'=(1/2)(\alpha'-\alpha)$ are yielding $\int g_1(\alpha')g_2(\alpha')\,\mathrm{d}\alpha'$.

If

$$f(n_i,\eta)=N_i^{-1/2}\sin\left[\frac{n_i\pi}{b}\left(\eta+\frac{b}{2}\right)\right],\quad g_1(\alpha')=N_1^{-1/2}\sin\left[\frac{n_i\pi}{2b}(\alpha+\alpha'+b)\right],$$

$$g_2(\alpha')=N_2^{-1/2}\sin\left[\frac{n_2\pi}{2b}(\alpha'-\alpha+b)\right] \tag{A5}$$

$$\Rightarrow g_1(\alpha')g_2(\alpha')=\frac{N_1^{1/2}N_2^{-1/2}}{2}\left\{\cos\left[\frac{(n_1-n_2)\pi}{2b}\left(\alpha'+b+\frac{\alpha}{\gamma}\right)\right]\right.$$

$$\left.-\cos\left[\frac{(n_1+n_2)\pi}{2b}(\alpha'+b+\alpha\gamma)\right]\right\},\quad \gamma=\frac{n_1-n_2}{n_1+n_2}.$$

Then if $n_1\neq n_2$,

$$\int g_1(\alpha')g_2(\alpha')\,\mathrm{d}\alpha'=\frac{N_1^{-1/2}N_2^{1/2}b}{\pi(n_1-n_2)}\sin\left[\frac{(n_1-n_2)\pi}{2b}\left(\alpha'+b+\frac{\alpha}{\gamma}\right)\right]$$

$$-\frac{N_1^{-1/2}N_2^{-1/2}b}{\pi(n_1+n_2)}\sin\left[\frac{(n_1+n_2)\pi}{2b}(\alpha'+b+\alpha\gamma)\right], \tag{A6a}$$

while if $n_1=n_2$,

$$\int g_1(\alpha')g_2(\alpha')\,\mathrm{d}\alpha'=N_1^{-1/2}N_2^{-1/2}\left\{\frac{\alpha'}{2}\cos\frac{n_1\pi\alpha}{b}-\frac{b}{2\pi n_1}\sin\frac{n_1\pi}{b}(\alpha'+b)\right\}. \tag{A6b}$$

Let

$$\Phi_1(n_1,n_2,\alpha)=\int_{-b-\alpha}^{b+\alpha}g_1(\alpha')g_2(\alpha')\,\mathrm{d}\alpha',\quad \Phi_2(n_1,n_2,\alpha)=\int_{-b+\alpha}^{b-\alpha}g_1(\alpha')g_2(\alpha')\,\mathrm{d}\alpha'. \tag{A7}$$

Then for $n_1\neq n_2$,

$$\Phi_1(n_1,n_2,\alpha)=\frac{N_1^{-1/2}N_2^{-1/2}b}{\pi}\left\{(n_1-n_2)^{-1}\right.$$

$$\times\left[\sin\frac{(n_1-n_2)\pi}{2b}\left(2b+\alpha+\frac{\alpha}{\gamma}\right)-\sin\frac{(n_1-n_2)\pi}{2b}\left(\frac{\alpha}{\gamma}-\alpha\right)\right]$$

$$\left.-(n_1+n_2)^{-1}\left[\sin\frac{(n_1+n_2)\pi}{2b}(2b+\alpha+\alpha\gamma)-\sin\frac{(n_1+n_2)\pi}{2b}(\alpha\gamma-\alpha)\right]\right\}, \tag{A8a}$$

$$\Phi_2(n_1, n_2, \alpha) = \frac{N_1^{-1/2} N_2^{-1/2} b}{\pi} \Bigg\{ (n_1 - n_2)^{-1} \times \left[\sin \frac{(n_1 - n_2)\pi}{2b} \left(2b - \alpha + \frac{\alpha}{\gamma} \right) - \sin \frac{(n_1 - n_2)\pi}{2b} \left(\frac{\alpha}{\gamma} + \alpha \right) \right] - (n_1 + n_2)^{-1} \left[\sin \frac{(n_1 + n_2)\pi}{2b} (2b - \alpha + \alpha\gamma) - \sin \frac{(n_1 + n_2)\pi}{2b} (\alpha\gamma + \alpha) \right] \Bigg\}, \tag{A8b}$$

while if $n_1 = n_2$,

$$\Phi_1(n, n, \alpha) = N_1^{-1/2} N_2^{-1/2} \left\{ (b + \alpha) \cos \frac{n_1 \pi \alpha}{b} - \frac{b}{2\pi n_1} \left[\sin \frac{n_1 \pi}{b} (\alpha + 2b) + \sin \frac{n_1 \pi \alpha}{b} \right] \right\}, \tag{A9a}$$

$$\Phi_2(n, n, \alpha) = N_1^{-1/2} N_2^{-1/2} \left\{ (b - \alpha) \cos \frac{n_1 \pi \alpha}{b} - \frac{b}{2\pi n_1} \left[\sin \frac{n_1 \pi}{b} (2b - \alpha) - \sin \frac{n_1 \pi \alpha}{b} \right] \right\}, \tag{A9b}$$

Finally, (Q_1, Q_2, Q_3, Q_4) in equation (A4) reduce to

$$\begin{aligned} Q_1 &= \int_{-b}^{0} \int_{-b}^{0} G(\alpha, \beta)\, \Phi_1(n_1, n_2, \alpha)\, \Phi_1(n_3, n_4, \beta)\, \mathrm{d}\alpha\, \mathrm{d}\beta, \\ Q_2 &= \int_{-b}^{0} \int_{-b}^{0} G(\alpha, \beta)\, \Phi_2(n_1, n_2, \alpha)\, \Phi_1(n_3, n_4, \beta)\, \mathrm{d}\alpha\, \mathrm{d}\beta, \\ Q_3 &= \int_{0}^{b} \int_{-b}^{0} G(\alpha, \beta)\, \Phi_1(n_1, n_2, \alpha)\, \Phi_2(n_3, n_4, \beta)\, \mathrm{d}\alpha\, \mathrm{d}\beta, \\ Q_4 &= \int_{0}^{b} \int_{0}^{b} G(\alpha, \beta)\, \Phi_2(n_1, n_2, \alpha)\, \Phi_2(n_3, n_4, \beta)\, \mathrm{d}\alpha\, \mathrm{d}\beta \end{aligned} \tag{A10}$$

and are evaluated numerically.